

# Finite Strain Tube-Squash Test of Concrete at High Pressures and Shear Angles up to 70 Degrees

by Zdenek P. Bazant, Jang Jay H. Kim, and Michele Brocca

*Although the existing triaxial tests and confined uniaxial-strain compression tests achieve high pressures, they cannot achieve large shear strains or deviatoric normal strains that are observed in some types of collapse of structures caused by missile impact, explosions, and earthquakes, or in explosive injection of anchors. A new type of concrete test, called the tube-squash test, that achieves, without fracturing under high pressures, enormous shear, and deviatoric strains, is developed.*

*Tubes 76.2 and 63.5 mm (3.0 and 2.5 in.) in diameter, with wall thicknesses of 14.22 and 12.7 mm (0.56 and 0.50 in.), made of highly ductile steel alloy, are filled with concrete. After curing, they are squashed in a high-capacity compression testing machine to 1/2 their original length, forcing the tubes to bulge. Normal and high-strength concretes at hydrostatic pressures of approximately 125 MPa (15,630 psi) are found to be remarkably ductile, capable of sustaining shear angles over 70 degrees without visually detectable cracks or voids, though significant distributed mechanical damage does take place. Tests of cores drilled out from squashed tubes show that, after such enormous deformation, the concrete still retains approximately 25 to 35% of its initial uniaxial compression strength and initial stiffness, and approximately 10 to 20% of its initial split-cylinder tensile strength.*

*What makes the tube-squash test meaningful is the development of a relatively simple method of test results analysis that avoids solving the inverse nonlinear finite strain problem with finite elements despite high nonuniformity of the strain field. Approximate stress-strain diagrams of concrete at such large shear angles and strains are obtained by finite strain analysis of the middle cross section utilizing the measured lateral expansion, axial shortening, and bulge profile. The finite strain triaxial plastic constitutive law of the steel alloy needs to be determined first, and a method to do that is also formulated. Approximate stress-strain diagrams and internal friction angles of concrete are deduced from the test without making any hypotheses about its constitutive equation. Tests of tubes filled by hardened portland cement paste and cement mortar, as well as tubes with a snugly-fitted limestone insert, show similar ductile shear strains and residual strengths. A separate paper documents good agreement of the present simplified method with finite element analysis.*

**Keywords:** concretes; ductility; strains.

## INTRODUCTION

In a small zone in front of the nose of an impacting hard missile, concrete is subjected to triaxial stress states with extremely high hydrostatic pressures and undergoes extreme deviatoric and shear strains far beyond the range of strains in the material tests that are available in the literature for calibrating the constitutive relation. Finite element modeling of such impact events requires knowledge of the finite-strain constitutive relations for such large strains. The same is true of explosive driving of anchors into concrete walls and, to a smaller extent, of blast effects on concrete structures.

As has been known for a long time (Woolson 1905), confinement in a steel tube makes concrete capable of plastic flow. The effect of confining pressure on the stress-strain curves was

demonstrated by Richart et al. (1929). Later, many experiments were conducted to explore the ductile behavior of concrete under high confining pressures; for example, the classical standard triaxial tests by Balmer (1949) or Green and Swanson (1973), or the recent tests at WES (1990), as well as numerous compression tests of concrete columns reinforced by spiral or ring stirrups (Burdette and Hillsdorf 1971). The importance of inducing high ductility of concrete by high confining pressures was emphasized by many authors (MacGregor 1988; Nilson and Winter 1979; Park and Paulay 1975). Recently, confinement by glass or carbon fibers or polymer fiber composites has received much attention (Kurt 1978; Fardis et al. 1981; Saadatmanesh et al. 1994; Picher et al. 1996; Kanatharana et al. 1998; and Burgueno et al. 1998). The hydrostatic stress-strain relations of concrete and hardened cement paste, up to record pressures of 2069 MPa (300,000 psi), were determined experimentally in confined uniaxial-strain compression tests by Bazant et al. (1986).

Various recent and ongoing finite element simulations indicate that strains of approximately 100% may occur in the case of impact or explosive injection of anchors, and 30% in the case of blast. Columns collapsed in earthquakes show strains up to roughly 15%. Such strain magnitudes are far larger than those achieved in the experimental studies of constitutive equations that generally do not exceed several percent. The current computational practice relies on constitutive relations that were experimentally calibrated for such small strains only. The degree of fictitious intuitive extrapolation of these constitutive relations beyond the range of existing experimental evidence is enormous. In the hydrocodes (wave codes) used to analyze missile impact, the plastic-fracturing constitutive models calibrated by material tests with shear angles of only a few degrees are used for deviatoric strains of approximately 100%.

Aware of the problem, the analysts adjust the large-strain extrapolation of the constitutive relation according to the measurements on hardened structures subjected to impact or blast. However, because many phenomena and factors intervene in dynamic collapse of entire structures, such adjustments are speculative and inevitably quite uncertain. A simple static test is needed that would yield comprehensive constitutive information more directly, without too many extraneous influences present.

The objectives of this study are to achieve:

1. A novel type of experiment in which very large pressures make it possible to produce without fracturing deviatoric strains with shear angles up to 70 degrees; and
2. A simplified procedure by which approximate stress-strain relations can be deduced from the test results without

ACI Materials Journal, V. 96, No. 5, September-October 1999.  
Received June 18, 1998, and reviewed under Institute publication policies. Copyright © 1999, American Concrete Institute. All rights reserved, including the making of copies unless permission is obtained from the copyright proprietors. Pertinent discussion will be published in the July-August 2000 ACI Materials Journal if received by April 1, 2000.

Zdenek P. Bazant, F-ACI, is Professor of Civil Engineering at Northwestern University, Evanston, Ill. He is a member of Joint ACI-ASCE Committees 334, Concrete Shell Design and Construction, and 4+7, Finite Element Analysis of Reinforced Concrete, and a member of ACI Committees 209, Creep and Shrinkage in Concrete; 231, Properties of Concrete at Early Ages; and 446, Fracture Mechanics.

Jang Jay H. Kim is a graduate research assistant in the Department of Civil Engineering at Northwestern University.

Michele Brocca is a graduate research assistant in the Department of Civil Engineering at Northwestern University.

having to tackle the difficult inverse problem of finite element analysis in finite strain.

The latter objective is crucial. Without it, the former would make no sense.

Achieving these two objectives would have considerable engineering significance. They would be useful for simulating: 1) impact and penetration of missiles into concrete walls; 2) blast and other explosion effects on concrete structures; 3) explosive driving of anchors into concrete walls; and 4) complete failure process of highly confined concrete columns in an earthquake. A similar test should be useful for some problems with rock (e.g., the tectonic processes deep in earth mantle), and other materials as well.

It must be emphasized that the following test data evaluation is only crude and approximate. An idea of the magnitude of error will be obtained once the inverse problem of fitting the data with a finite strain finite element program is tackled. This is not an easy task.

## EXPERIMENTAL METHOD

A thick-walled tube made of highly ductile steel alloy that can sustain strains of approximately 100% without cracking was filled with concrete (or cement paste or other material to be tested). The filled tube was then placed in a high-capacity testing machine and was compressed between two rigid platens to approximately 50% of its original length (Fig. 1(a)). In the process, the steel tube expanded laterally and bulged in the middle (Fig. 1 and 2). As a companion test, an empty steel tube was also squashed in the same manner to determine the properties of the steel (Fig. 3(a)). The axial force-displacement diagram and the expansion of the diameter at the midlength of the tube during loading and unloading were measured.

Specimens that were cut, as seen in Fig. 3(b), show the difference of the internal shapes of the filled and empty tubes. The difference is obviously caused by the pressures that the concrete filling applies on the tube.

After removing the squashed tube specimens from the testing machine, two types of examination were conducted. Some specimens were cut and the surface of concrete was examined visually (Fig. 4). Although the possibility of attaining good ductility in concrete by high confining pressure has been well-known, the strain magnitude that can be attained without any visually observable damage is, at first, startling. Even after undergoing a shear angle over 70 degrees, the surface of a cut in concrete showed no voids or fractures (Fig. 4).

A coring machine was used to drill out cores from the remaining specimens in the axial direction (Fig. 5). These cylindrical cores were then subjected either to the uniaxial compression test or to the Brazilian split cylinder test. The tests yielded the stress-strain curves, compression strength, and splitting tensile strength of the highly deformed concrete. It is remarkable that the compression strength after squashing was still approximately 30% of its original value.

The concept of these tube-squash tests is to use a highly ductile steel alloy tube of a large wall thickness, capable of providing

**Table 1—Number of steel tubes filled with different material for larger-(I) and smaller-(II) diameter tubes**

	Set I	Set II
Normal strength concrete	10	10
High-strength concrete	10	10
Cement paste	—	10
Mortar	—	10
Dry aggregate and sand	—	2
Limestone	—	3
Steel tube only	5	5
Total number of tubes	25	50

**Table 2—Mixture content of each material per dm<sup>3</sup>\***

Content	HSC	NSC	Cement paste	Cement mortar
Cement, Type I, N	4.28	3.32	14.6	11.0
Pea, maximum 1/4 in., N	9.53	9.31	—	—
Sand, No. 2, N	0.10	8.70	—	13.97
S. F. slurry, N	1.19	—	—	—
Water, N	1.09	1.97	166.3	4.71
Superplasticizer, cm <sup>3</sup>	160.0	—	—	—

\*1 dm<sup>3</sup> = 0.001 m<sup>3</sup>.

extreme confining pressures, to allow the specimen to bulge as it is compressed, and to conduct companion tests of empty steel tubes to identify the finite-strain constitutive properties of the steel. This concept, however, would be useless if no clear and simple method of evaluation existed. Thus the main idea, which makes the tube-squash test meaningful, is how to easily extract useful approximate information from the observed nonuniform deformation of the specimen. A simplified method to do that is presented herein.

Verification of the current simplified method of evaluations requires solving the inverse material identification problem with a finite-strain finite element code. This will be reported separately (Brocca and Bazant 1999).

## BASIC CHARACTERISTICS OF EXPERIMENTS

Two series of tests were carried out using steel alloy tubes of two different diameters whose dimensions are shown in Fig. 1(a). The tubes were made of steel alloy ASTM No. 1020. The normal strength concrete had a maximum aggregate size of 9.52 mm (0.375 in.) and an average uniaxial compression strength  $f'_c = 41.37$  MPa (6000 psi). The mixture proportions of concrete at casting are shown in Table 1. The high-strength concrete had a maximum aggregate size of 9.52 mm (0.375 in.), and an average uniaxial compression strength  $f'_c = 86.19$  MPa (12,500 psi). The specimens were cast and cured at room temperature in a water bath for 28 days, after which they were tested.

The tests were carried out at constant rate of axial displacement, which was  $2.54 \times 10^{-2}$  mm/s (0.001 in./s). A rate higher than  $2.54 \times 10^{-2}$  mm/s (0.001 in./s) was found to be impossible because it caused the steel tube to crack. Twenty five specimens of 73.2 mm (3.0 in.) diameter and 50 specimens of 63.5 mm (2.5 in.) diameter were tested. The mixtures of the different types of material cast in the tube are listed in Table 2. The diameters of the cores drilled out of the specimens of the larger and smaller diameters were 30.5 mm (1.245 in.) and 25.4 mm (0.995 in.), respectively. In Series 2 (smaller diameter), two of the tubes tested were filled with aggregate and sand, and three with a snugly fitting core of Indiana limestone. Mineralogically, the larger aggregates were clean P-gravels composed mostly of dolomite, granite, and basalt, with traces of quartz and metamorphic rock (schist). The sand used was the normal No. 2 sand.

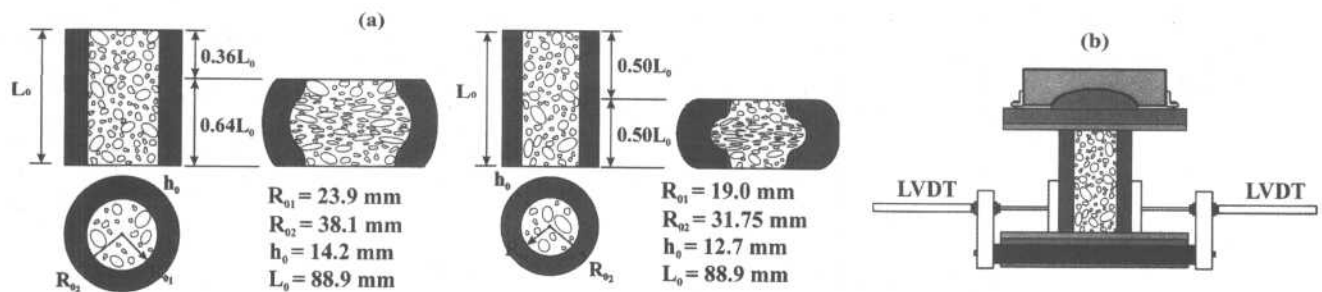


Fig. 1—(a) Dimensions and geometry of filled specimens before and after squash-tube test; and (b) test setup and placement of linear variable displacement transducer (LVDT) gages to measure change of diameter.

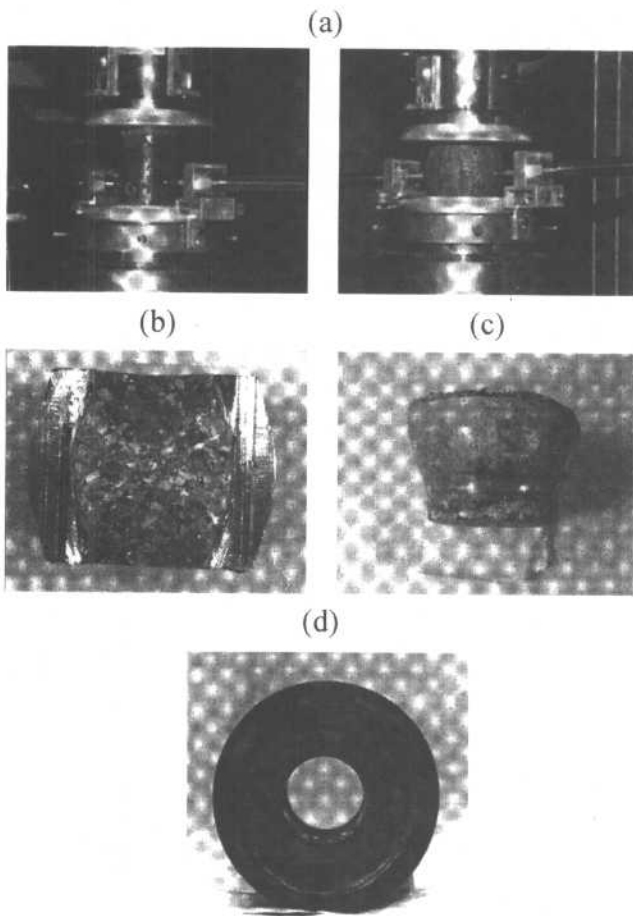


Fig. 2—(a) Test setup before and after squash-tube test of filled specimens; (b) cut large diameter specimen in which formation of diagonal shear band can be discerned; (c) part of squashed concrete fill after deformed steel tube cut off; and (d) squashed specimen after coring out cylinder sample of fill.

Figure 2(a) shows a photograph of the compression test of the filled tube specimen before and after deformation. Figure 4 shows the axial cut through a specimen of high strength concrete squashed to 50% of its original length. Note the rearrangement and flattening of the aggregate pieces caused by shortening the tube to 1/2 the length. No visual cracks or voids are apparent even though initially orthogonal diagonals have changed their angle by 70 degrees. Formation of diagonal shear bands can be detected in Fig. 2(b). Figure 2(c) demonstrates the integrity of a bell-shaped end piece of a specimen of normal concrete deformed by 36% after it has been removed from the deformed tube, cut normally to the axis.

Figure 6(a) and 7 show, on the right, the diagrams of axial load versus the axial displacement between the specimen ends

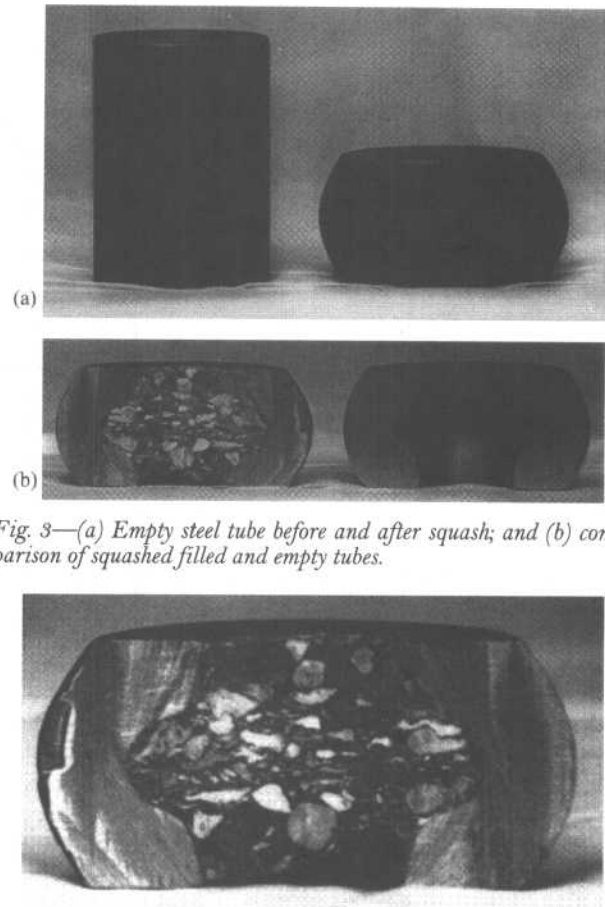


Fig. 3—(a) Empty steel tube before and after squash; and (b) comparison of squashed filled and empty tubes.



Fig. 4—Microstructure seen on axial cut of filled high-strength specimen squashed to 50% of initial length.

and, on the left, the lateral displacement (i.e., the increase of diameter during the tube-squash test) during the squash test of larger- and smaller-diameter tubes, respectively. For each tube-squash test, the maximum lateral displacement is continuously measured by a linear variable differential transformer (LVDT), as shown in Fig. 1(b). Both graphs also include similar test data for the unfilled steel tubes. The corresponding diagrams of the axial stress versus the axial strain and the lateral strain for the larger- and smaller-diameter tubes are shown in Fig. 6(b) and 7(b), respectively. To avoid the clutter of too many curves, only a single data set is selected from each type of smaller filled tube specimens and is plotted in Fig. 7(b).

Figure 2(d) shows a squashed filled tube of the smaller diameter from which a core has been drilled out; a hole in the remaining concrete is visible. For comparison tests, identical cores were drilled out of virgin concrete specimens cast from the same batch of concrete. Figure 5(a) through (d) shows pairs of the cores extracted from normal concrete, high-strength concrete,

**Table 3—Compression and tension test results of core specimens from larger-diameter filled tube specimens**

		Compression					
		Deformed			Virgin		
		$L$ , cm	$P_{fail}$ , N	$f'_c$ , MPa	$L$ , cm	$P_{fail}$ , N	$f'_c$ , MPa
Normal strength concrete		2.48	7477	9.51	3.47	29,654	37.73
		2.50	6427	8.17	3.92	26,305	33.47
		2.55	9798	12.47	3.97	25,340	32.24
		2.58	11,449	14.56	3.98	24,428	31.08
		—	—	—	5.32	27,977	35.60
		—	—	—	5.76	27,595	35.11
		—	—	—	5.78	24,677	31.40
High-strength concrete		3.68	18,299	23.28	3.54	69,032	87.85
		3.69	18,272	23.25	3.76	74,815	95.20
		3.70	17,493	22.26	3.91	73,703	93.79
		3.75	18,863	24.00	4.03	67,075	85.35
		3.79	18,557	23.61	5.52	69,184	88.04
		—	—	—	5.58	57,107	72.67
		—	—	—	5.69	60,430	76.90
		Tension					
		Deformed			Virgin		
		$L$ , cm	$P_{fail}$ , N	$f'_t$ , MPa	$L$ , cm	$P_{fail}$ , N	$f'_t$ , MPa
Normal strength concrete		2.08	689	0.66	1.67	6062	7.29
		2.17	240	0.22	1.87	5506	5.92
		—	—	—	2.25	8580	7.65
		—	—	—	2.27	9910	8.76
High-strength concrete		1.74	1619	1.87	1.75	13,953	15.99
		2.67	3278	2.46	1.80	15,287	17.05
		2.86	3602	2.53	2.80	21,034	15.10
		2.93	2299	1.57	2.86	22,791	15.99

cement mortar, and hardened cement paste. The deformed concrete is on the left of each pair, and the virgin concrete is on the right. Figure 4 shows the axial cuts through a deformed specimen of high-strength concrete (of Series 2) and through an unfilled steel tube. Note the damaged midsections of the deformed normal and high-strength concrete where the aggregates are flattened and layered.

Figure 8(a) and (c) show the recorded diagrams of axial load versus relative displacement between the ends of specimen for cores of virgin and deformed material, for normal strength and high-strength concrete from the larger-diameter filled tube specimens. The corresponding axial stress normalized by the average compressive strength of virgin material versus axial strain diagrams are shown in Fig. 8(c) and (d). Figure 9(a) exhibits the diagrams of load versus displacement of specimen for cores of virgin and deformed material, for normal strength concrete, high-strength concrete, cement mortar, and cement paste from the smaller-diameter tubes. The corresponding normalized stress-strain diagrams are shown in Fig. 9 (b).

For the normal and high-strength concrete cores from both the larger- and smaller-diameter tubes, the maximum compression strength of the deformed cores is reduced to approximately 1/3 compared to the virgin cores. For the cement paste and the cement mortar cores from the smaller-diameter filled tubes, the maximum compression strengths are approximately 65 and 25%, respectively, of the corresponding virgin core strengths. The initial axial stiffness is reduced in approximately the same ratio for all the core specimens. The results of all the compression tests of cores from the larger-diameter tubes are tabulated in Table 3, and from the smaller-diameter tubes, in Table 4.

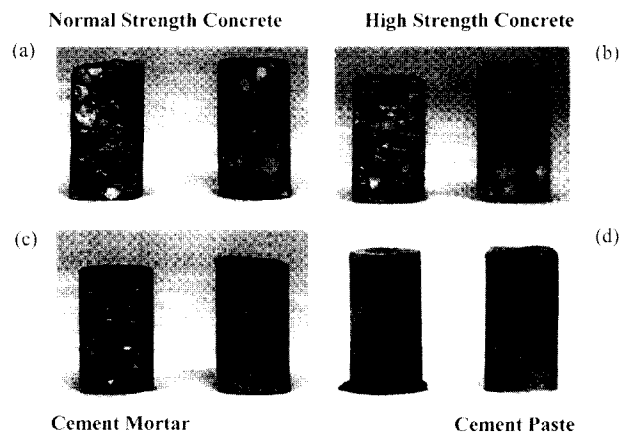


Fig. 5—Cores of squashed and virgin material of: (a) normal strength concrete; (b) high-strength concrete; (c) cement mortar; and (d) cement paste.

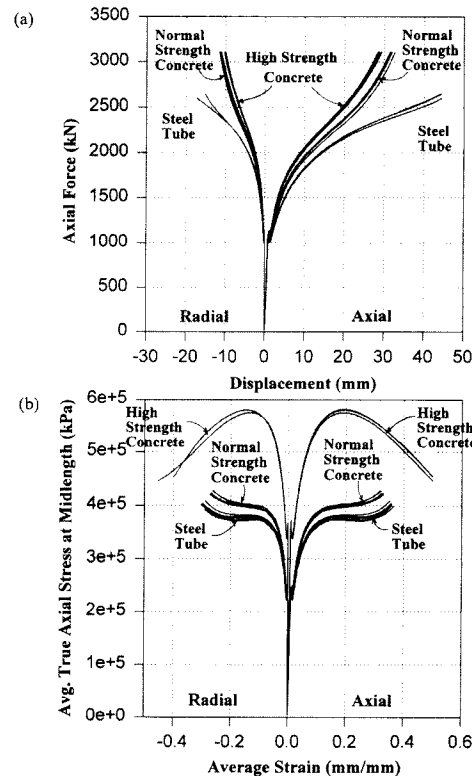


Fig. 6—(a) Axial force versus axial and radial displacements for larger-diameter filled tubes; (b) average true axial stress at midlength versus average axial and radial strains for larger-diameter filled tubes.

The results of the split-cylinder Brazilian tests giving approximate tensile strengths of both the virgin and deformed cores taken from the larger- and smaller-diameter filled tubes are given in Table 3 and 4, respectively. Generally, the values of the splitting tensile strength were extremely scattered, and, on the average, represent approximately 20 to 30% of the tensile strength of the virgin specimens.

Conducting the tube-squash tests for many different thicknesses of the steel tube is beyond the scope of this study. Especially interesting would be the large deformation of tubes with much smaller wall thicknesses, in which the confining pressures are not high enough to prevent fracturing, which takes place already at small shear angles (several degrees only). Although thin tubes would not be expected to yield essential new information

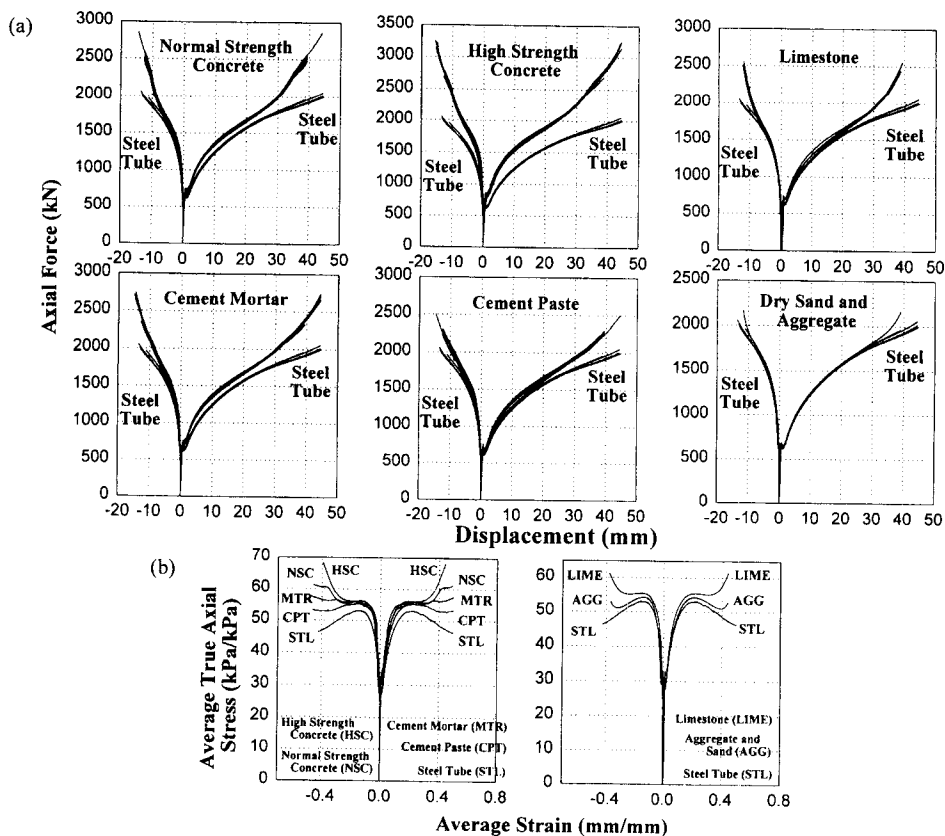


Fig. 7—(a) Axial force versus axial and radial displacements for smaller-diameter filled tubes; and (b) average true axial stress at midlength versus axial and radial strains for smaller-diameter filled tubes.

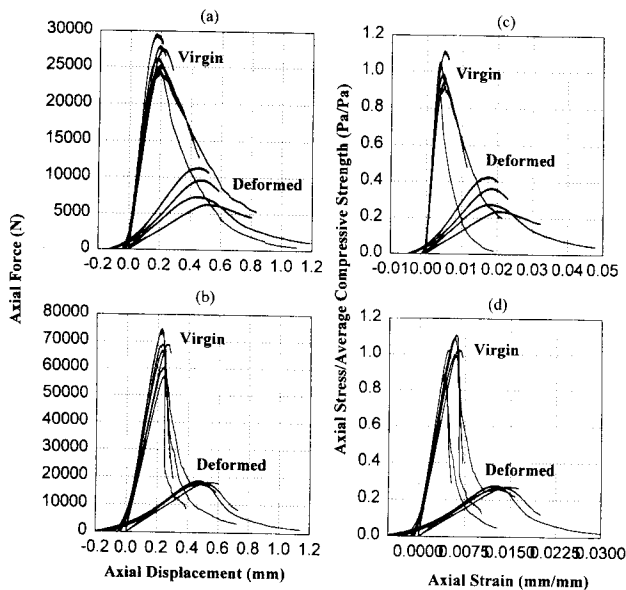


Fig. 8—Axial forces in: (a) normal; and (b) high-strength concrete cores versus axial displacement for cores taken from larger-diameter tubes, both deformed and virgin. Axial stresses in: (c) normal; and (d) high-strength concrete cores versus axial strains for cores taken from larger-diameter tubes, both deformed and virgin.

on the plastic response of concrete, which is the focus of this study, they would yield the constitutive properties of concrete reduced to rubble. The rubbleized concrete would behave essentially as gravel and its behavior would have to be described by large-strain constitutive models of soil mechanics type.

Fortunately, for the large-strain behavior of ductile steel alloys, well-proven models exist. It is generally accepted that the

von Mises yield surface is adequate even at very large strains (e.g., the model of Johnson and Cook [1983]). Due to this fact, it will suffice to calibrate the scalar hardening function of steel at large strains, which will be done herein by the test of the empty tube.

### APPROXIMATE STRESS CALCULATION WITH FINITE STRAIN ANALYSIS

In finite strain experiments involving large shear deformations, it seems inevitable to accept specimens that deform non-uniformly, as is the case for the present tube-squash test. Because of nonuniformity of strain, an accurate evaluation of stresses and strains in the specimen is a very difficult inverse problem of nonlinear finite element analysis. The difficulty is aggravated by the finiteness of strains, which means the problem involves both the physical and geometric nonlinearities. By exploiting measured finite deformations, however, it is possible to carry out an approximate analysis under some simplifying, but probably reasonable, assumptions.

A thin circular ring element at midlength of the deformed tube is considered having, after deformation, a small thickness  $h$ . The stress and strain fields are axisymmetric in both steel and concrete. The authors assume the axial and circumferential stresses  $\sigma_1$  and  $\sigma_2$  to be uniformly distributed along the radius within the steel part, as well as the concrete part of the element, and the radial stress  $\sigma_3$  to be uniform in concrete but vary linearly with the radial coordinate  $r$  in steel (Fig. 10(b)). The shear stresses in this element all vanish for  $h \rightarrow 0$  because of symmetry. This means that the stresses acting on the faces of the ring are the principal stresses, and the strains are the principal strains.

In finite strain theory (Malvern 1969; Ogden 1984; and Bazant and Cedolin 1991), the deformation gradient tensor  $F$  is decomposed as  $F = RU$ , in which  $R$  = rotation tensor; and  $U$  =

**Table 4—Compression and tension test results of core specimens from smaller-diameter filled tube specimens**

Compression						
	Deformed			Virgin		
	$L, \text{ cm}$	$P_{fail}, \text{ N}$	$f'_c, \text{ MPa}$	$L, \text{ cm}$	$P_{fail}, \text{ N}$	$f'_c, \text{ MPa}$
Normal strength concrete	4.44	5617	11.53	6.03	21,559	44.28
	3.89	9452	19.41	6.03	18,677	38.36
	3.55	6391	13.12	6.03	19,170	39.37
	3.51	8535	17.53	—	—	—
High-strength concrete	4.00	22,809	46.84	5.96	52,170	107.15
	3.98	22,831	46.89	5.90	51,085	104.92
	2.94	19,980	41.03	5.90	49,937	102.56
	2.85	32,172	66.07	5.96	56,409	115.85
Cement mortar	4.23	20,945	43.02	5.96	29,174	59.92
	4.24	21,426	44.00	5.90	29,877	61.36
	4.64	19,660	40.38	5.96	30,513	62.67
	4.64	19,722	40.50	5.96	30,139	61.90
Cement paste	4.49	5702	11.71	6.03	33,867	69.55
	4.50	13,913	28.57	5.96	36,228	74.40
	3.88	11,079	22.75	6.03	31,616	64.93

Tension						
	Deformed			Virgin		
	$L, \text{ cm}$	$P_{fail}, \text{ N}$	$f'_c, \text{ MPa}$	$L, \text{ cm}$	$P_{fail}, \text{ N}$	$f'_c, \text{ MPa}$
Normal strength concrete	2.38	3251	3.48	2.03	9007	11.32
	2.43	3451	3.61	2.05	8126	10.09
	2.28	2419	2.71	2.64	12,080	11.68
	—	—	—	2.66	10,977	10.52
High-strength concrete	2.08	7201	8.84	2.15	20,878	24.71
	2.65	9065	8.73	2.18	20,723	24.25
	1.92	6970	9.29	2.73	25,473	23.84
	1.66	4496	6.91	2.54	25,202	23.16
Cement mortar	2.64	8962	8.67	—	—	—
	2.13	11,164	13.37	2.44	13,553	15.63
	2.47	15,007	15.49	2.22	13,206	15.18
	2.41	15,185	16.09	2.62	15,883	15.44
Cement paste	2.41	16,070	17.02	2.61	16,760	16.29
	1.56	7957	13.02	2.19	12,992	15.12
	1.24	7859	16.14	2.18	14,567	17.04
	1.21	7134	14.96	2.48	14,389	14.77
2.62	10,719	10.42	2.52	16,808	17.00	

tensor characterizing the deformation and called the right-stretch tensor. It is further convenient to decompose the deformation into its volumetric and deviatoric components. This is done in finite strain theory by a multiplicative decomposition  $U = U_D U_V$ , in which  $U_D, U_V$  are the right-stretch tensors for the separate deviatoric and volumetric deformations (an additive decomposition can be introduced as a good approximation [Bazant 1996]; however, it is not needed it for the present purpose.)

In the symmetrically deforming ring that has been introduced (Fig. 10(a)), there is no rotation, i.e.,  $R = I$  and  $F = U$ . Therefore, and because the axes  $x_1, x_2,$  and  $x_3$  shown in Fig. 10(a) are the principal axes (representing the axial direction of the cylinder and the tangential and radial directions of the circular wall)

$$F = U = \begin{bmatrix} \lambda_1 & 0 & 0 \\ 0 & \lambda_2 & 0 \\ 0 & 0 & \lambda_3 \end{bmatrix} = \begin{bmatrix} \lambda_1/\lambda & 0 & 0 \\ 0 & \lambda_2/\lambda & 0 \\ 0 & 0 & \lambda_3/\lambda \end{bmatrix} \begin{bmatrix} \lambda & 0 & 0 \\ 0 & \lambda & 0 \\ 0 & 0 & \lambda \end{bmatrix} \quad (1)$$

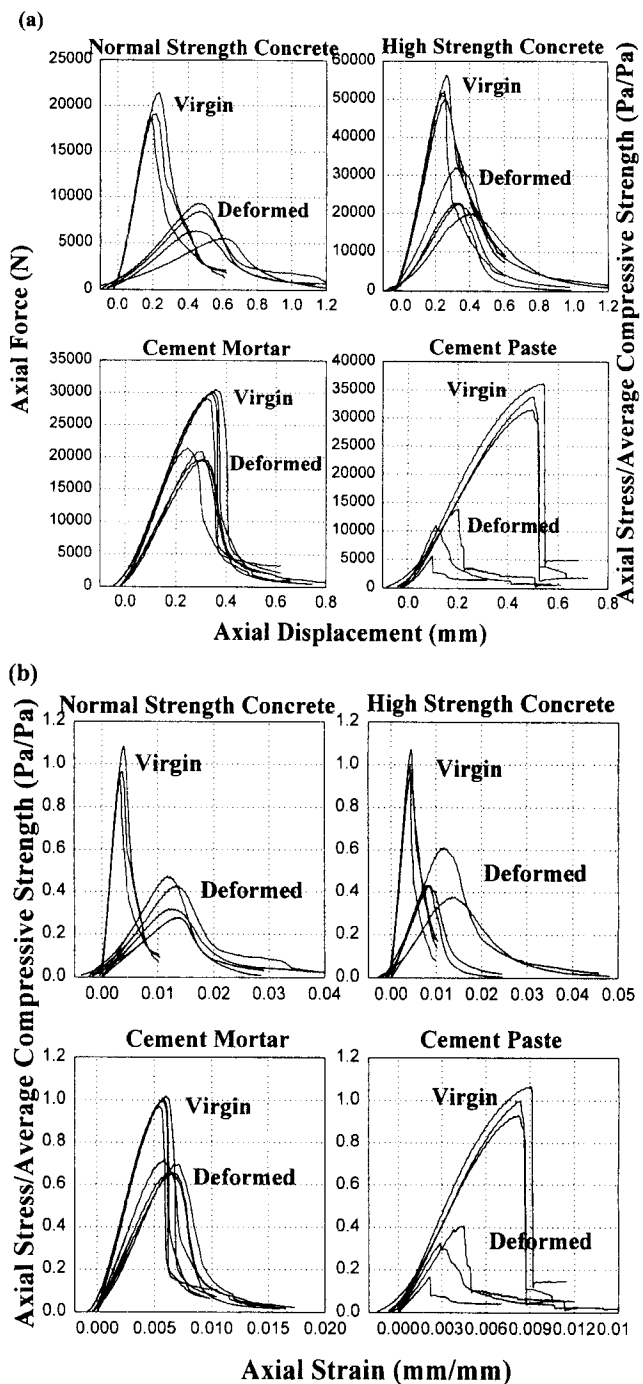


Fig. 9—Axial forces in (a) normal, and (b) high-strength concrete cores versus axial displacement for cores taken from smaller-diameter tubes, both deformed and virgin. Axial stresses in (c) normal, and (d) high-strength concrete cores versus axial strains for cores taken from smaller-diameter tubes, both deformed and virgin.

in which  $\lambda_1, \lambda_2,$  and  $\lambda_3 =$  principal stretches in the directions of  $x_1, x_2,$  and  $x_3$  (i.e., the ratios of the deformed length to the initial length of a material segment), and  $\lambda = J^{1/3}, J = \lambda_1 \lambda_2 \lambda_3$  where  $J = \det F =$  Jacobian of the deformation.

The work of stresses on the deformations of a material element of an initially unit volume may be written as

$$W = (\lambda_2 \lambda_3 \sigma_1) d\lambda_1 + (\lambda_3 \lambda_1 \sigma_2) d\lambda_2 + (\lambda_1 \lambda_2 \sigma_3) d\lambda_3 \quad (2)$$

$$= (J\sigma_1) d\ln\lambda_1 + (J\sigma_2) d\ln\lambda_2 + (J\sigma_3) d\ln\lambda_3, (J = \lambda^3)$$

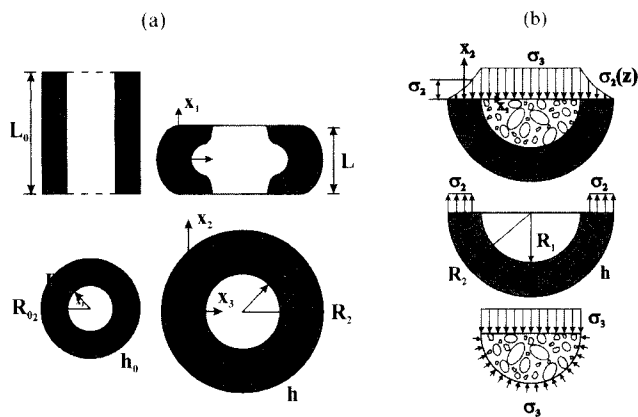


Fig. 10—(a) Notations and coordinates used in analysis; and (b) stress distributions considered in analysis.

Herein,  $\sigma_i$  ( $i = 1, 2, 3$ ) are the components of the Cauchy (true) stress tensor with respect to the vertical, circumferential, and radial coordinate axes  $x_i$ . They represent the forces acting on an element of a current unit volume cut out from the deformed material.  $(\lambda_2 \lambda_3 \sigma_1)$ ,  $(\lambda_3 \lambda_1 \sigma_2)$ , and  $(\lambda_1 \lambda_2 \sigma_3)$  represent the forces acting on an element that was a unit element before the deformation, having enlarged the areas of its unit faces from 1 to  $\lambda_2 \lambda_3$ ,  $\lambda_3 \lambda_1$ , and  $\lambda_1 \lambda_2$ . The last expression in Eq. (2) is convenient because the subscripts 1, 2, and 3 are separated in each term. Therefore, it is expedient to introduce as a measure of strain as the Hencky strain (also called the logarithmic strain, recently discussed in Bazant 1998). Its principal values are  $\gamma_i = \ln \lambda_i$  ( $i = 1, 2, 3$ ), and its volumetric component is  $\gamma_V = \ln \lambda = (\ln J)/3 = (\gamma_1 + \gamma_2 + \gamma_3)/3$ . The deviatoric Hencky strains may be defined as  $\gamma_{Di} = \ln(\lambda_i/\lambda) = \gamma_i - \gamma_V$ .  $J \sigma_i$  are the principal values of what is known as the Kirchhoff stress tensor.

The stresses and strains in the concrete element will be labeled by superscript C, and those in the steel element will have no labels. The stress-strain relations must be written in terms of conjugate strains and stresses, i.e., stress and strain measures that, together, give the correct expression for work  $W$ , as in Eq. (2). As is well-known and confirmed by Eq. (2), this may be achieved by writing the stress-strain relation as a relation between the logarithmic strain and the Kirchhoff stress (this is possible because there is no rotation; if there was rotation, a more general approach would be needed). The steel can be described by Hencky's total strain theory of plasticity. Thus, in view of material isotropy, one may write the stress-strain relation for the steel alloy in the form

$$\gamma_V = \frac{\lambda^3 \sigma_V}{3K}, \quad \gamma_{Di} = \frac{f(\bar{\gamma}^p)}{2G} \lambda^3 \sigma_{Di} \quad (3)$$

in which

- $K, G$  = bulk and shear elastic moduli (for small strains);
- $\lambda^3$  =  $\lambda_1 \lambda_2 \lambda_3 = J$  and  $\sigma_V = (\sigma_1 + \sigma_2 + \sigma_3)/3$ ;
- $\sigma_{Di}$  =  $\sigma_i - \sigma_V$ ;
- $\sigma_i; \sigma_{Di}$  ( $i = 1, 2, 3$ ) = the volumetric component and deviatoric components of the Cauchy (true) stress tensor;
- $\bar{\gamma}^p$  = suitable plastic hardening parameter; and
- $f(\bar{\gamma}^p)$  = function that describes plastic hardening, such that  $f(0) = 1$  if, initially,  $\bar{\gamma}^p = 0$ .

The deviatoric (or isochoric) stretch tensor  $U$  may be decomposed into its elastic part  $U^{eD}$  and plastic part  $U^p$ , while the volumetric stretch tensor  $U^V$  is purely elastic, and needs no decomposition. Because  $\lambda_i = (\lambda_i/\lambda_i^e) \lambda_i^e = (\lambda_i/\lambda_i^e) (\lambda_i^e/\lambda) \lambda$ , the following can be written

$$F = U = U^p U^e = U^p U^{eD} U^V = \quad (4)$$

$$\begin{bmatrix} \lambda_1/\lambda_1^e & 0 & 0 \\ 0 & \lambda_2/\lambda_2^e & 0 \\ 0 & 0 & \lambda_3/\lambda_3^e \end{bmatrix} \begin{bmatrix} \lambda_1^e/\lambda & 0 & 0 \\ 0 & \lambda_2^e/\lambda & 0 \\ 0 & 0 & \lambda_3^e/\lambda \end{bmatrix} \begin{bmatrix} \lambda & 0 & 0 \\ 0 & \lambda & 0 \\ 0 & 0 & \lambda \end{bmatrix}$$

in which  $U^e$  = total elastic stretch tensor. For Hencky strain, the elastic-plastic decomposition is additive,  $\gamma_i = \ln \lambda_i = \ln \lambda_i^p + \ln \lambda_i^e = \gamma_i^p + \gamma_i^e$ .

The plastic hardening of metals may be assumed to be governed by the second invariant  $J_2$  of the deviatoric stress or strain tensor. The latter is found to give more reasonable results for the present problem. Therefore, the hardening parameter is considered as the so-called plastic strain intensity (an invariant) that is generalized to finite Hencky strain, as follows

$$\bar{\gamma}^p = \sqrt{J_2(\gamma_i^p)} = \quad (5)$$

$$\sqrt{[(\gamma_1^p - \gamma_2^p)^2 + (\gamma_2^p - \gamma_3^p)^2 + (\gamma_3^p - \gamma_1^p)^2]/6}$$

in which the plastic Hencky strains  $\gamma_i^p = \ln \lambda_i^p$  are calculated as

$$\gamma_i^p = \ln \lambda_i - \gamma_i^e, \quad \gamma_i^e = \left( \frac{1}{9K} + \frac{1}{2G} \right) \sigma_V + \frac{1}{2G} \sigma_i, \quad (i = 1, 2, 3) \quad (6)$$

Combining the volumetric and deviatoric stress-strain relations (Eq. (3)), the total stress-strain relations for the steel may be written as  $F_1 = 0$ ,  $F_2 = 0$ , and  $F_3 = 0$  where

$$F_1 = \left[ \left( \frac{1}{9K} + \frac{f(\bar{\gamma}^p)}{3G} \right) \sigma_1 + \quad (7)$$

$$\left( \frac{1}{9K} - \frac{f(\bar{\gamma}^p)}{6G} \right) (\sigma_2 + \sigma_3) \right] \lambda_1 \lambda_2 \lambda_3 - \ln \lambda_1$$

$$F_2 = \left[ \left( \frac{1}{9K} + \frac{f(\bar{\gamma}^p)}{3G} \right) \sigma_2 + \quad (8)$$

$$\left( \frac{1}{9K} - \frac{f(\bar{\gamma}^p)}{6G} \right) (\sigma_3 + \sigma_1) \right] \lambda_1 \lambda_2 \lambda_3 - \ln \lambda_2$$

$$F_3 = \left[ \left( \frac{1}{9K} + \frac{f(\bar{\gamma}^p)}{3G} \right) \sigma_3 + \quad (9)$$

$$\left( \frac{1}{9K} - \frac{f(\bar{\gamma}^p)}{6G} \right) (\sigma_1 + \sigma_2) \right] \lambda_1 \lambda_2 \lambda_3 - \ln \lambda_3$$

The strategy in evaluating the stresses in concrete is to first calculate the approximate stresses in steel and then obtain the approximate stresses in concrete from equilibrium conditions, avoiding any hypothesis about the constitutive relations for concrete. The constitutive properties of the steel need to be

evaluated in advance from the squash test of an empty tube, which was analyzed first.

The circumferential stretch in the steel is approximately characterized by the stretch of the middle circle of the wall (Fig. 11(a) through (d)),  $\lambda_2 = [(R_1 + R_2)/2] / [(R_{1_0} + R_{2_0})/2]$  where  $R_1, R_2$  = inner and outer radii of the deformed ring, and subscript 0 labels the initial undeformed values. The circumferential and radial stretches satisfy the geometric conditions  $F_4 = 0$  and  $F_5 = 0$  where

$$F_4 = R_1 + R_2 - (R_{1_0} + R_{2_0})\lambda_2, \quad F_5 = R_1 - R_2 + \lambda_3 h_0 \quad (10)$$

and  $h_0 = R_{2_0} - R_{1_0}$  = initial wall thickness.

The evolution of the inner and outer radii of the deformed tube at midlength  $R_1$  and  $R_2$  is needed in the previous equations. During the test, only the variation of  $R_2$  as a function of  $L$  was measured. The initial value  $R_{1_0}$  and the final value  $R_{1_1}$  of  $R_1$  were also measured. It is assumed that  $R_1$  grows from its initial value to its final value linearly with  $R_2$

$$R_1 = R_{1_0} + (R_{1_1} - R_{1_0})\chi, \quad \chi = \frac{R_2 - R_{2_0}}{R_{2_1} - R_{2_0}} \quad (11)$$

The axial equilibrium condition of the ring provides the equation  $F_6 = 0$  in which

$$F_6 = \pi(R_2^2 - R_1^2)\sigma_1 + \pi R_1^2 \sigma_1^C - P \quad (12)$$

where  $P$  = applied axial force (negative for compression). On the inner surface of the tube, the radial normal stress must be equal to the internal pressure  $p$ .

The locations of the resultants of the axial compressive stresses  $\sigma_1$  in all the horizontal cross sections of the tube form the compression line. Initially, this line is straight and passes through elements in Fig. 11(b) because the axial stress is initially uniform. But when the tube bulges, bending moments may develop, causing the axial stress distribution throughout the thickness of tube to become nonuniform and the resultant to move away from the centroid. Thus, the compression line may become curved, but with a different curvature than the outer surface. Approximately, it may be assumed as a parabolic arc, of rise  $\delta$  in the middle (Fig. 1(a)). The curvature of the arc is  $\kappa = 8\delta/L^2$ . Due to this curvature, there is a distributed radial force  $p_r = \kappa\sigma_1(R_2 - R_1)$  that must be balanced by the hoop stresses  $\sigma_2$ .

To formulate the radial force equilibrium condition of the ring element, a small angular sector of the ring of central angle  $d\phi$  (Fig. 11(a) and (b)) and height  $dx$  are considered. Summing the radial (outward) components of all the forces on the ring sector,  $pR_1 dx d\phi - 2\sigma_2(d\phi/2)(R_2 - R_1)dx + p_r(R_1 + R_2)/2 dx d\phi = 0$ . After substitutions for  $p_r$  and  $\kappa$ , one achieves the condition  $F_7 = 0$  where

$$F_7 = \sigma_2 + \frac{\kappa}{2}(R_1 + R_2)\sigma_1 - \frac{R_1}{R_2 - R_1}p \quad (13)$$

where  $\sigma_1$  = average axial stress in the cross section, and  $p$  = pressure on the inner surface of the deformed steel tube, which is zero if the tube is empty. The term with  $\kappa$  may be regarded as the nonlinear geometric effect of buckling of the wall due to the axial force.

There seems to be no simple way to estimate the curvature  $\kappa$ . Therefore,  $\kappa$  may be considered as an unknown in the analysis

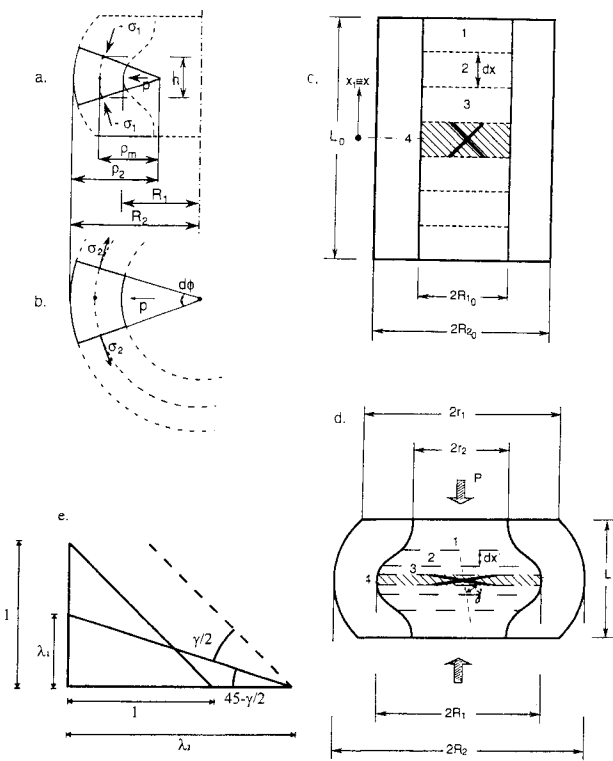


Fig. 11—(a) Axial, and (b) circumferential stresses acting on ring element of squashed steel tube at midlength; (c) initial; and (d) deformed configurations of filled tube, showing change of angle of two initially orthogonal diagonals; and (e) relation of shear angle to length changes corresponding to principle stretches.

of the empty tube, and the  $\kappa$ -values obtained may be used later in the analysis of the filled tube (however, the values of  $\kappa$  in the computations appeared to be very small, not larger than the perceived error of the analysis, and so they were neglected in the analysis of the filled tube; i.e.,  $\kappa \approx 0$ ).

The radial normal stress in an internally pressurized tube may vary across the thickness approximately linearly. This means that, for the tube filled by concrete, the equilibrium condition at the inner surface may be approximated as  $2\sigma_3 = -p$  or  $F_8 = 0$  where

$$F_8 = 2\sigma_3 + p \quad (14)$$

and  $\sigma_3$  = radial stress at midthickness.

One might wonder whether Eq. (13) should not involve the stresses referred to the initial undeformed configuration (Bazant and Cedolin, Chapter 11), such as Biot stresses that are obtained by rotating the stresses  $S_1 = \lambda_2\lambda_3\sigma_1$ ,  $S_2 = \lambda_3\lambda_1\sigma_2$ , instead of the Cauchy stresses  $\sigma_1$  and  $\sigma_2$ . The area transformations involved in the expressions for Biot stresses, however, are already included in Eq. (13) by means of the deformed radii  $R_1, R_2$  and the rotations through angles  $\kappa h/2$  and  $d\phi$ .

1. *Steel in empty tube*—In this case,  $\sigma_1^C = 0$  and  $p = 0$ . At each stage of loading,  $R_2$  and  $P$  are measured. Seven variables need to be solved:  $X_1 = \lambda_1$ ,  $X_2 = \lambda_2$ ,  $X_3 = \lambda_3$ ,  $X_4 = \sigma_1$ ,  $X_5 = \sigma_2$ ,  $X_6 = \kappa$ , and  $X_7 = f(\gamma^p)$ . The conditions  $F_i = 0$  ( $i = 1, \dots, 7$ ) provide a system of seven nonlinear equations for these seven variables. They can be effectively solved by the Levenberg-Marquardt iterative nonlinear optimization algorithm, which minimizes the sum of squares  $\sum F_i^2 = \text{Min}$ . Ideally, the solution should converge to  $\text{Min} = 0$ , which then implies that  $F_i = 0$  for each  $i$ . Because of inevitable numerical errors,  $\text{Min} > 0$ , but if it is small enough, the right-hand side of each equation must be small enough, too, and an approximate solution may thus be reached.

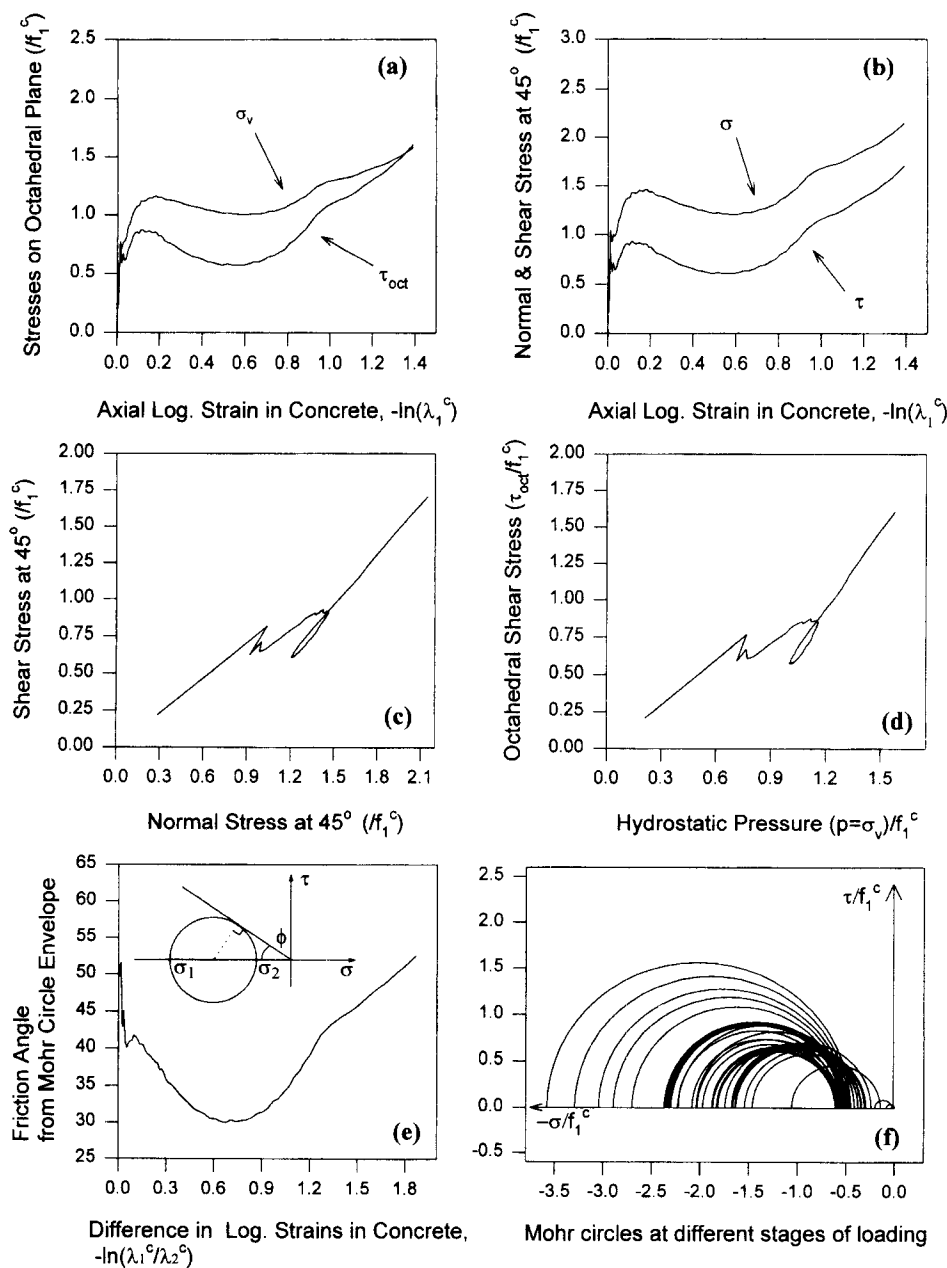


Fig. 12—Calculated stress-strain diagrams, paths in stress spaces, and friction characteristics exhibited by high-strength concrete in smaller-diameter tubes.

It would be possible to eliminate several variables and thus reduce the number of simultaneous nonlinear equations to solve. When dealing with such a small number of nonlinear equations, however, it poses no difficulty when this powerful computer algorithm is used. In practice, nothing would be gained by reducing the number of equations. What is, however, important for good convergence is to supply a good initial estimate of the solution at each loading stage. Fortunately, the current problem falls into a special class of nonlinear problems in which good estimates can be obtained by tracing the evolution of response. The solution obtained in one loading step may be used as a good enough initial estimate of the solution for the next loading step, provided that the loading step is small enough and that the random scatter of the measurements is eliminated by smoothing the histories of the measured variables. (Rather small loading steps are required to achieve convergence; in this case, 1,750 axial displacement increments needed to be used.)

After solving the histories of stresses,  $\bar{\gamma}^p$  may be further evaluated for each stage of loading and the plot (or table) of  $f(\bar{\gamma}^p)$  versus  $\bar{\gamma}^p$  may be constructed (Fig. 12(d)). If the plot contains roughness due to experimental scatter, it is suitable to smooth it out by a low-degree polynomial. A subroutine is written for evaluating the function  $f(\bar{\gamma}^p)$ . Alternatively, if the data are sufficiently smooth, interpolation from the discrete values may also be used in this subroutine.

2. Filled tube test—In the tube filled by concrete, a large radial pressure  $p$  is applied by concrete on the inner surface of the deformed tube. At each stage of loading of the filled tube,  $P$ ,  $L$ , and  $R_2$  is measured, and the inner radius  $R_1$  can be approximately evaluated in advance. Eight unknowns exist—six stretches and stresses in steel:  $\xi_1 = \lambda_1$ ,  $\xi_2 = \lambda_2$ ,  $\xi_3 = \lambda_3$ ,  $\xi_4 = \sigma_1$ ,  $\xi_5 = \sigma_2$ ,  $\xi_6 = \sigma_3$ , the axial stress in concrete  $\xi_7 = \sigma_1^c$ , and the pressure on the inner steel wall  $\xi_8 = p$ . We also have eight equations  $F_i(\xi_1, \dots, \xi_8) = 0$  ( $i = 1, \dots, 8$ ); they are Eq. (7), (8), (9), (10), and (13), supplemented by the known curvature function (for the present tests, however,  $k = 0$ ).

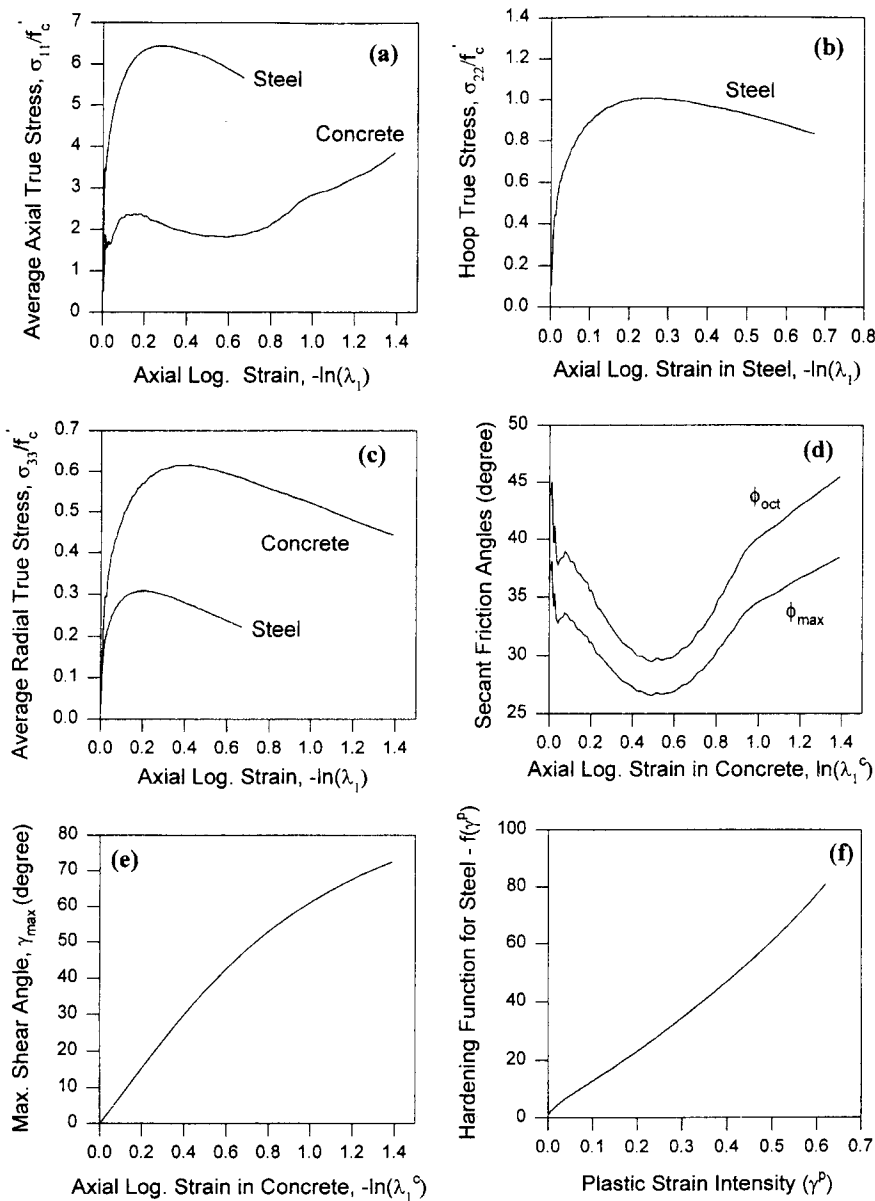


Fig. 13—(a) through (e) Calculated stress-strain diagrams exhibited during tube squash by high-strength concrete in smaller-diameter specimens (a through e); and (f) hardening function of plastic strain intensity of steel calibrated by empty tube squash.

In each loading step, the eight nonlinear equations are again solved by the Levenberg-Marquardt algorithm, using the solution from the previous loading step as the initial estimate. The horizontal principal normal stresses in the concrete element in the center of the tube are  $\sigma_2^C = \sigma_3^C = -p$ .

3. *Stretches of concrete*—After analyzing the test of the filled tube, one may determine the stretches of concrete at every stage of loading. As an approximation, the thin horizontal slices of the concrete filling, shown in Fig. 11(c), will be assumed to deform while keeping their cross sections plane, as in Fig. 11(d). This might not be a very good assumption for the local strains, but gives good, probable estimates of the average strains in each slice, which is what matters most. The principal stretches in concrete in the lateral directions may thus be assumed roughly uniform throughout the cross section plane. Thus, for the slice at midlength (cross-hatched in Fig. 11(c) and (d))

$$\lambda_2^C = \lambda_3^C = \frac{R_1}{R_{10}} \quad (15)$$

According to visual observation of an axial cut through the specimen, the principal stretch  $\lambda_1$  in the axial direction is distributed along the axis of cylinder rather nonuniformly, with axial strain concentration at the midlength (Fig. 11(d)). Obviously, the bulging of the specimen at midlength tends to increase the axial strain because the material can flow to the sides, while at the ends, this is not possible. The approximate shape of the distribution of  $\lambda_1$  may be estimated from the lateral stretches observed.

As a simple approximation, the hydrostatic stress  $\sigma_f^C$  in concrete, and thus also the relative volume change  $\lambda_f^C$  of concrete, may be considered to be uniform throughout the deformed concrete filling (because the shear stresses must be expected to be much smaller in magnitude, as is verified by Fig. 13(d)). Thus,  $\lambda_f^C$  times the initial volume  $\pi R_{10}^2 dx$  of a transverse slice (Fig. 11(c)) of initial thickness  $dx$ , located initially at axial coordinate  $x (= x_1)$  measured from the midlength, must be equal to the deformed volume of this slice, which may be written as  $\pi R_{10}^2(\xi) \lambda_1^C(\xi) dx$  where  $\xi = 2x/L_0 =$  dimensionless axial coordinate; hence

$$\lambda_1^C(\xi) = \frac{\lambda_V^C R_{10}^2}{R_1^2(\xi)} \quad (16)$$

The sum of the deformed thicknesses of all the slices (Fig. 11(d)) per 1/2 of the tube length must be equal to  $L/2$ , i.e.

$$\int_0^{L/2} \lambda_1^C(\xi) dx = L/2$$

Insert Eq. (16) and substitute new integration variable  $\xi$  for which  $dx = L_0 d\xi/2$  and the upper integration limit corresponding to  $x = L_0/2$  is  $\xi = 1$ . Thus

$$\lambda_V^C = \frac{L}{L_0 I}, I = \int_0^1 \left( \frac{R_{10}}{R_1(\xi)} \right)^2 d\xi \quad (17)$$

The value of this integral is best obtained numerically, e.g., by Simpson's integration rule.

Further, the simplifying assumption that the change of distribution of the inner radius  $R_1(x)$  along the height is approximately geometrically similar at all times is introduced, i.e.

$$R_1(\xi) - R_{10} = (R_1 - R_{10})\psi(\xi) \quad (18)$$

where  $R_1 = R_1(0) =$  inner radius at midlength, and  $\psi(\xi)$  is the same function for all stages at loading, with  $\psi(0) = 1$ ;  $\psi(\xi)$  may be measured on an axial cut of the specimen after the test.

Substitution of Eq. (17) into Eq. (16) provides for the stretch of concrete at midlength

$$\lambda_1^C = \frac{LR_{10}^2}{L_0 I R_1^2} \quad (19)$$

where  $L/L_0$  is the average axial stretch.

4. *Calculated stress-strain diagrams for concrete*—The stresses and strains in high-strength concrete obtained by the procedure previously described are shown in Fig. 13 (a) through (e) and Fig. 12 (a) through (d). These diagrams can be used for calibrating an approximate constitutive equation for concrete at high pressures and very large shear strains. Figure 13(f) shows the hardening function  $f(\gamma^p)$  for steel obtained from the analysis of the test of the empty steel tube.

Note from Fig. 13(e) that the maximum shear angle exceeds 70 degrees at the end of the test. The maximum confining pressure calculated at the center of the specimen is  $p = \sigma_3^C = \sigma_2^C = 51$  MPa (7400 psi). This appears to be the pressure needed to make concrete deform in a ductile manner without fracturing, but is probably not the overall maximum confining pressure because, due to bulging of the steel wall, the radial stress distribution is doubtless quite nonuniform and the sharp difference in axial curvatures of the inner wall surface of the filled and empty steel tubes could cause the maximum confining pressure to occur near the wall.

The maximum shear angle  $\gamma_{max}$  among planes of all orientations (which occurs on planes rotated by  $\pm 45$  degrees) is calculated easily from the distortion of an initially right-angled equilateral triangle shown in Fig. 11(e). Its unit sides change according to the stretches to  $\lambda_1$ , and  $\lambda_2$ . From the figure,  $\tan(45 \text{ degrees} - \gamma_{max}/2) = \lambda_1/\lambda_2$ , and so

$$\gamma_{max} = 90 \text{ degrees} - 2 \arctan(\lambda_1/\lambda_2) \quad (20)$$

The shear angle  $\gamma$  represents the change of angle between two initially orthogonal diagonals, shown as the dashed lines in Fig. 11(c) and (e), which transform to the two crossing inclined lines, shown as solid lines (Fig. 11(d)).

The maximum shear stress among planes of all orientations in concrete occurs on the plane inclined by 45 degrees and is  $\tau_{max} = (\sigma_1 - \sigma_2)/2$ . The normal stress on that plane is  $\sigma_n = (\sigma_1 + \sigma_2)/2$ . The secant friction angle  $\phi_{45}$  on that plane is (for  $\sigma_n < 0$ ) given by

$$\tan \phi_{45} = \frac{\tau_{max}}{\sigma_n} = \frac{\sigma_1 - \sigma_2}{\sigma_1 + \sigma_2} \quad (21)$$

Another measure of friction, of interest for classical Drucker-Prager type plasticity models based on stress invariants, is provided by the secant friction angle  $\phi_{oct}$  on the octahedral planes, which is given (for  $\sigma_r < 0$ ) by

$$\tan \phi_{oct} = \frac{\tau_{oct}}{|\sigma_{oct}|} = \frac{\sqrt{2J_2(\sigma_i)}/3}{|\sigma_r|} \quad (22)$$

$$= \frac{1}{|\sigma_r|} \sqrt{\frac{1}{9} [(\sigma_1 - \sigma_2)^2 + (\sigma_2 - \sigma_3)^2 + (\sigma_3 - \sigma_1)^2]}$$

The maximum secant friction angle  $\phi$  among planes of all orientations is, according to Mohr circle of stress (Fig. 12(e)), given by

$$\sin \phi = \frac{\sigma_1 - \sigma_2}{\sigma_1 + \sigma_2} \quad (23)$$

Figure 13(d) shows the calculated plot of  $\phi_{oct}$  and  $\phi_{max}$  versus  $\ln \lambda_1^C$ , and Fig. 12 (a) and (b) show the calculated plots of  $\tau_{max}$ ,  $\phi_n$ ,  $\tau_{oct}$ , and  $\sigma_r$  as a function of  $\ln \lambda_1^C$ .

Furthermore, Fig. 12(c) and (d) show the calculated plots of  $\tau_{max}$  versus  $\sigma_r$  on the maximum shear stress plane, and of  $\tau_{oct}$  versus  $\sigma_r$  on the octahedral plane. The little steep jumps and loops in these plots are caused by the softening, as shown in Fig. 13(a) and (b). The initial and final slopes of the plot in Fig. 12(c) indicate, for those planes, incremental internal friction angles of 38 and 45 degrees for the maximum stress plane, and those in Fig. 12(d) indicate 50 and 61 degrees for the octahedral plane.

Figure 12(e) shows the evolution of the maximum secant friction angle  $\phi$  (obtained from Mohr circle) as a function of  $\ln \lambda_1^C$  and of hydrostatic pressure  $p = -(\sigma_1 + 2\sigma_2)/3$ . Its maximum and minimum values in the inelastic range are

$$\phi_{max} = 50 \text{ degrees}, \quad \phi_{min} = 30 \text{ degrees} \quad (24)$$

Finally, Fig. 12(f) shows Mohr circles of the stress states during the loading process. This is not the actual Mohr envelope because only one loading path has been tested.

### Finite element verification of simplified method of evaluation

In a parallel study to be published separately (Brocca and Bazant 1999), finite-strain finite element analysis was conducted to assess the accuracy of the current simplified evaluation of test results. To model the tube at large deformations, a microplane constitutive model for steel (with a kinematic constraint) was

developed in a form that is, in the case of proportional straining, equivalent to von Mises plasticity. The hardening function of the constitutive model on the microplanes was calibrated by matching the observed deformations of the steel tube. A very close match was achieved.

Subsequently, the recently developed microplane model (Bazant et al. 1999) was adopted for concrete, and its formulation was extended to arbitrarily large finite strains (without cracking). For certain physical reasons, however, nonconjugate measures of finite strain tensor and Lagrangian stress tensor were used (namely, Green's strain tensor and back-rotated Cauchy stress tensor), the dissipation inequality was always satisfied. The material parameters of this microplane model, except the compression strength, were not adjusted to optimize the fits. Rather, their values were taken the same as determined in previous calibration by triaxial, biaxial, and uniaxial test results. Thus, the response of concrete was predicted rather than optimized (Bazant et al. 1986). In spite of that, the present simplified analysis of the measurements shows reasonable agreement with the finite element predictions, especially their final values. The largest differences found are shown in Fig. 14, but even those are acceptable. For the average axial stress in the cross section, the agreement is closer.

It may be concluded that the present simplified method of evaluation of large deformation test results very likely has sufficient accuracy for practical purposes. It was surprising that the confining pressures that caused the concrete in the present tests to deform plastically, without any visible cracking, are not extremely high. They have the same order of magnitude as the uniaxial compression strength, although values several times larger were intuitively expected before the tests. These surprising results are verified by the finite element analysis. Without the finite element verification, the present simplified method could not be recommended with high confidence.

Since the microplane model was found to correctly predict the behavior of plasticized concrete within the present thick tubes, this model may also be used to predict the behavior of concrete at weaker confinement, as in thinner tubes, but only as long as fracturing does not occur.

## CONCLUSIONS

1. Measuring the response of concrete at very large shear (or deviatoric) strains and pressures is feasible if a test is accepted in which the deformation of the specimen is highly nonuniform. The penalty is a more difficult, though not greatly difficult, identification of the constitutive relation.

2. While the triaxial compression tests and the confined compression tests with uniaxial strain can achieve only high pressures and not large strains, the presently proposed tube-squash test can achieve very large shear angles exceeding 70 degrees.

3. At hydrostatic pressures 1.5 times standard uniaxial compression strength, the normal and high-strength concrete can sustain shear angles over 70 degrees without any visible damage. The uniaxial compression strength after such deformation drops to approximately 25 to 35% of the initial value, and the split-cylinder tensile strength drops to approximately 10 to 20% of the initial value, as measured on small-diameter drilled cores. The Young's elastic modulus after this large deformation decreases to approximately 25 to 35% of its initial value.

4. Approximate stress-strain diagrams can be identified from the measured axial displacement, axial force, and change of diameter by simplified finite strain analysis, provided that the constitutive properties of the ductile steel alloy are calibrated by a separate large deformation squash test of an empty tube. The properties of steel can be approximately described by an isotropic Hencky total strain plasticity model formulated in terms of the Hencky (logarithmic) strains and Kirchhoff conju-

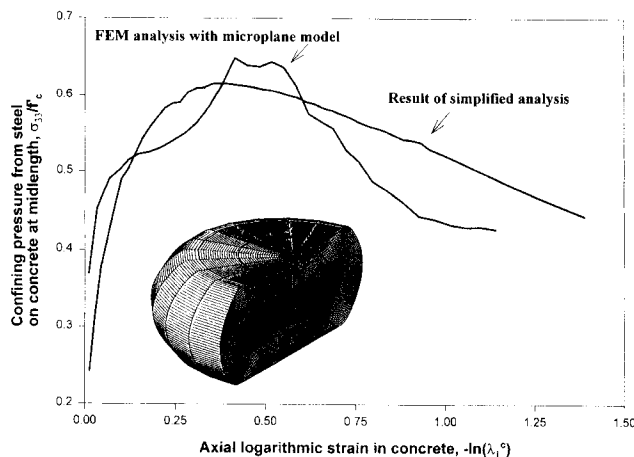


Fig. 14—Comparison of present simplified evaluation of confining radial pressure with prediction by finite element analysis (Brocca and Bazant 1999) (reason curves terminate at different strains is that the finite element analysis gives a larger axial strain at steel surfaces at midheight that simplified analysis).

gate stresses, with a function depending on finite strain intensity. The lateral confining stresses in concrete can then be estimated by equilibrium analysis of the middle cross section of the specimen.

5. Approximate analysis of concrete behavior in the tests indicates that the hydrostatic pressure reaches approximately  $1.5f'_c$ , amounting to approximately 330 MPa (48,000 psi), and that the principal stress difference that can be sustained at these pressures is approximately 280 MPa (40,000 psi). At such pressures, the diagram of axial stress versus axial strain for concrete shows softening within the range  $0.2 < \ln\lambda_1^C < 0.6$  and rehardening for  $-\ln\lambda_1^C > 0.6$ . On the maximum shear stress planes, the secant friction angle varies approximately from 27 to 38 degrees, and the incremental friction angle from 38 to 45 degrees. On the octahedral stress planes, the friction angle varies in the inelastic range from 30 to 45 degrees. The maximum secant angle internal friction obtained from the Mohr circle varies in the inelastic range from 30 to 50 degrees.

6. Finite-strain finite element analysis reported separately confirms that the present simplified method of evaluation of test results very likely has sufficient accuracy.

## ACKNOWLEDGMENTS

Partial financial support under Contract D CA-96K-0049 between Waterways Experiment Station (WES), Vicksburg, Miss., and Northwestern University (monitored by J. Zelasko) is gratefully acknowledged. Additional partial funding for the experiments was obtained from the ACBM Center at Northwestern University.

## REFERENCES

- ASTM, 1995, *Annual Book of ASTM Standards for Construction: Concrete and Aggregates*, Section 4, V. 04.02.
- Balmer, G.G., 1949, "Shearing Strength of Concrete under High Triaxial Stress—Computation of Mohr's Envelope as a Curve," *Report SP-23*, Structural Research Laboratory, Bureau of Reclamation, U.S. Department of the Interior, Denver, Colo., Oct., 26 pp.
- Bazant, Z. P., 1996, "Finite Strain Generalization of Small-Strain Constitutive Relations for Any Finite Strain Tensor and Additive Volumetric-Deviatoric Split," *International Journal of Solids and Structures*, 33 (20-22), pp. 2887-2897.
- Bazant, Z. P., 1998, "Easy-to-Compute Tensors with Symmetric Inverse Approximating Hencky Finite Strain and Its Rate," *Journal of Materials of Technology*, ASME 120, Apr., pp. 131-136.
- Bazant, Z. P., and Cedolin, L., 1991, *Stability of Structures: Elastic, Inelastic, Fracture and Damage Theories*, Oxford University Press, New York.
- Bazant, Z. P.; Bishop, F. C.; and Chang, T.-P., 1986, "Confined Compression Tests of Cement Paste and Concrete up to 300 ksi" *ACI JOURNAL*, *Proceedings* V. 83, No. 4, July-Aug., pp. 553-560.
- Bazant, Z. P., and Prat, P. C., 1988, "Microplane Model for Brittle Plastic

Material: II Verification," *ASCE Journal of Engineering Mechanics*, V. 114, pp. 1689-1702.

Brocca, M., and Bazant, Z. P., 1999, "Inverse Finite-Strain Finite Element Analysis of 'Tube-Squash' Test of Concrete with Shear Angles up to 70 Degrees," *Report*, Northwestern University. (in preparation)

Burdette, E. G., and Hilsdorf, H. K., 1971, "Behavior of Laterally Reinforced Concrete Columns," *Journal of the Structural Division*, ASCE 97, Feb., pp. 587-602.

Burgueno, R.; Davol, A.; and Seible, F., 1998, "Carbon Shell System for Modular Bridge Components," *Fiber Composites in Infrastructure*, Proceedings of the 2nd International Conference, ICCI, Tucson, H. Saadatmanesh and M. R. Ehsani, eds., University of Arizona, Tucson, pp. 341-354.

Fardis, N. M., and Khalili, M., 1981, "Concrete Encased in Fiberglass-Reinforced Plastics," *ACI JOURNAL*, *Proceedings* V. 78, No. 6, Nov.-Dec., pp. 440-446.

Green, S. J., and Swanson, S. R., 1973, "Static Constitutive Relations for Concrete," *Report* No. AFWLTR-72-2, Air Force Weapons Lab, Kirkland Air Force Base.

Johnson, G. R., and Cook, W. H., 1983, "Constitutive Model and Data for Metals Subjected to Large Strains, High Strain Rates, and High Temperatures," *Proceedings of the 7th International Symposium on Ballistics*, The Hague, The Netherlands.

Kanatharana, J., and Lu, L.-W., 1998, "Strength and Ductility of Concrete Columns Reinforced by FRP Tubes," *Fiber Composites in Infrastructure*, Proceedings of the 2nd International Conference, ICCI, Tucson, H. Saadatmanesh and M. R. Ehsani, eds., University of Arizona, Tucson, pp. 370-384.

Kurt, C. E., 1978, "Concrete-Filled Structural Plastic Columns," *Journal of the Structural Division*, ASCE 104 (ST1), pp. 55-63.

Levenberg, K., 1944, "Method for the Solution of Certain Nonlinear Problems in Least-Squares," *Quart. Applied Math.*, V. 2, pp. 164-168.

MacGregor, J. G., 1988, *Reinforced Concrete: Mechanics and Design*, Prentice Hall, Englewood Cliffs, N.J.

Malvern, L. E., 1969, *Introduction to the Mechanics of a Continuous Medium*, Prentice Hall, Englewood Cliffs, N.J.

Marquardt, D. W., 1963, "An Algorithm for Least-Squares Estimation of Nonlinear Parameters," *Journal of Soc. Industr. Appl. Math.*, V. 11, pp. 431-441.

Miriam, A.; Kargahi, M.; Samaan, M.; and Shahawy, M., 1996, "Composite FRP-Concrete Column with Bidirectional External Reinforcement," 1996, *Fiber Composites in Infrastructure*, Proceedings of the 1st International Conference, ICCI, Tucson, H. Saadatmanesh and M. R. Ehsani, eds., University of Arizona, Tucson, pp. 888-902.

Nilson, A. H., and Winter, G., 1979, *Design of Concrete Structures*, McGraw-Hill, New York.

Park, R., and Paulay, T., *Reinforced Concrete Structures*, John Wiley and Sons, Inc., New York, 1975.

Picher, F., Rochette, P.; and Labossière, P., 1996, "Confinement of Concrete Cylinders with CFRP" 1996, *Fiber Composites in Infrastructure*, Proceedings of the 1st International Conference, ICCI, Tucson, H. Saadatmanesh and M. R. Ehsani, eds., University of Arizona, Tucson, pp. 829-841.

Richart, F. E.; Brandzaeg, A.; and Brown, R. L., 1929, "Failure of Plain and Spirally Reinforced Concrete in Compression," *Engineering Experiment Station Bulletin* No. 190, University of Illinois, Urbana, Ill., 79 pp.

Saadatmanesh, H.; Ehsani, M. R.; and Li, M. W., 1994, "Strength and Ductility of Concrete Columns Externally Reinforced by Fiber Composite Straps," *ACI Structural Journal*, V. 91, No. 4, July-Aug., pp. 434-447.

WES, Concrete Triaxial Test Data Contained in Bazant, Z. P., Xiang, Y., Adley, M. D., Prat, P. C., and Akers, S. A., 1996, "Microplane Model for Concrete, Part II: Data Delocalization and Verification," *Journal of Engineering Mechanics*, ASCE, V. 122, No. 3, 1971, pp. 255-262.

Woolson, I. H., 1905, "Some Remarkable Tests Indicating Flow of Concrete under Pressure," *Engineering News*, V. 54, No. 18, pp. 459-460.